RESEARCH ARTICLES

PLANETARY SCIENCE

The geology of Pluto and Charon through the eyes of New Horizons

Jeffrey M. Moore,[1]* William B. McKinnon,[2] John R. Spencer,[3] Alan D. Howard,[4] Paul M. Schenk,[5] Ross A. Beyer,[6,1] Francis Nimmo,[7] Kelsi N. Singer,[3] Orkan M. Umurhan,[1] Oliver L. White,[1] S. Alan Stern,[3] Kimberly Ennico,[1] Cathy B. Olkin,[3] Harold A. Weaver,[8] Leslie A. Young,[3] Richard P. Binzel,[9] Marc W. Buie,[3] Bonnie J. Buratti,[10] Andrew F. Cheng,[8] Dale P. Cruikshank,[1] Will M. Grundy,[11] Ivan R. Linscott,[12] Harold J. Reitsema,[3] Dennis C. Reuter,[13] Mark R. Showalter,[6] Veronica J. Bray,[14] Carrie L. Chavez,[6,1] Carly J. A. Howett,[3] Tod R. Lauer,[15] Carey M. Lisse,[8] Alex Harrison Parker,[3] S. B. Porter,[3] Stuart J. Robbins,[3] Kirby Runyon,[8] Ted Stryk,[16] Henry B. Throop,[17] Constantine C. C. Tsang,[3] Anne J. Verbiscer,[18] Amanda M. Zangari,[3] Andrew L. Chaikin,[19] Don E. Wilhelms,[20] New Horizons Science Team

NASA's New Horizons spacecraft has revealed the complex geology of Pluto and Charon. Pluto's encounter hemisphere shows ongoing surface geological activity centered on a vast basin containing a thick layer of volatile ices that appears to be involved in convection and advection, with a crater retention age no greater than ~10 million years. Surrounding terrains show active glacial flow, apparent transport and rotation of large buoyant water-ice crustal blocks, and pitting, the latter likely caused by sublimation erosion and/or collapse. More enigmatic features include tall mounds with central depressions that are conceivably cryovolcanic and ridges with complex bladed textures. Pluto also has ancient cratered terrains up to ~4 billion years old that are extensionally faulted and extensively mantled and perhaps eroded by glacial or other processes. Charon does not appear to be currently active, but experienced major extensional tectonism and resurfacing (probably cryovolcanic) nearly 4 billion years ago. Impact crater populations on Pluto and Charon are not consistent with the steepest impactor size-frequency distributions proposed for the Kuiper belt.

We present a preliminary geological examination of Pluto and Charon based on images and other data collected by NASA's New Horizons spacecraft during its flyby of these worlds on 14 July 2015. The two camera systems pertinent to geological investigations are the wide-angle color Multispectral Visible Imaging Camera (MVIC) and the narrow-angle panchromatic Long Range Reconnaissance Imager (LORRI) (*1*). This paper focuses on the portions of the illuminated surfaces seen near closest approach at better than 1 km/pixel resolutions, centered on 180° longitude for Pluto and 0° longitude for Charon (*2*, *3*). All topographic measurements were obtained using stereo photogrammetric techniques, supplemented by preliminary photoclinometry and shadow and limb measurements (*4*). An acronym list is provided in the supplementary materials. All feature names used in this paper are informal, and the locations of named features on Pluto and Charon are shown in figs. S1 and S2, respectively; terrain locations are indicated in fig. S3.

[1]National Aeronautics and Space Administration (NASA) Ames Research Center, Space Science Division, Moffett Field, CA 94035, USA. [2]Department of Earth and Planetary Sciences, Washington University in St. Louis, St. Louis, MO 63130, USA. [3]Southwest Research Institute, Boulder, CO 80302, USA. [4]Department of Environmental Sciences, University of Virginia, Charlottesville, VA 22904, USA. [5]Lunar and Planetary Institute, Houston, TX 77058, USA. [6]The SETI Institute, Mountain View, CA 94043, USA. [7]University of California, Santa Cruz, CA 95064, USA. [8]Johns Hopkins University Applied Physics Laboratory, Laurel, MD 20723, USA. [9]Massachusetts Institute of Technology, Cambridge, MA 02139, USA. [10]NASA Jet Propulsion Laboratory, Pasadena, CA 91019, USA. [11]Lowell Observatory, Flagstaff, AZ 86001, USA. [12]Stanford University, Stanford, CA 94305, USA. [13]NASA Goddard Space Flight Center, Greenbelt, MD 20771, USA. [14]University of Arizona, Tucson, AZ 85721, USA. [15]National Optical Astronomy Observatory, Tucson, AZ 85719, USA. [16]Roane State Community College, Oak Ridge, TN 37830, USA. [17]Planetary Science Institute, Tucson, AZ 85719, USA. [18]Department of Astronomy, University of Virginia, Charlottesville, VA 22904, USA. [19]Independent Science Writer, Arlington, VT 05250, USA. [20]U.S. Geological Survey, Retired, Menlo Park, CA 94025, USA.
*Corresponding author. E-mail: jeff.moore@nasa.gov

Pluto

Pluto's surface exhibits an astonishing variety of landscapes (Fig. 1A). Broadly, the encounter hemisphere (EH) contains several regional provinces: (i) the ~1000-km-wide uncratered plain, Sputnik Planum (SP), centered on the EH; (ii) arcuate, rugged-to-mountainous regions surrounding SP on three sides; (iii) mantled and eroded plains at higher latitudes; and (iv) a heterogeneous surface west of SP containing plains with various degrees of crater density and surface texture, scarps (both erosional and tectonic), troughs (graben), and patches of rugged cratered terrain.

Sputnik Planum and environs

This ~870,000-km^2 oval-shaped unit of high-albedo plains, centered at ~20°N, 175°E, is likely a massive unit of volatile ices (solid N_2, CO, and CH_4) (*5*), the level of which is 3 to 4 km below the surrounding uplands. The central and northern regions of SP display a distinct cellular pattern (*5*), which varies in appearance across the planum. In the bright central portion (fig. S4A), the cells are bounded by shallow troughs up to 100 m deep (*5*); the centers of at least some cells are elevated by ~50 m relative to their edges, though some apparently have less relief. The southern region and eastern margin of SP do not display cellular morphology, instead showing featureless plains and dense concentrations of pits, themselves reaching a few kilometers across (fig. S4D). Details of the different morphologies encountered within SP are described in the supplementary materials.

No impact craters have been confirmed on SP in contiguous mapping coverage at 390 m/pixel scale. Following the arguments in (*5*), the crater retention age of SP is very young (≲10 million years old) and is discussed in the supplementary materials. Such geologically recent resurfacing and/or topographic relaxation is consistent with the weak rheology of N_2-dominated ices (*6*, *7*) and with the interpretation of cells as expressions of potentially active solid-state convection in a thick layer of such ices (supplementary materials).

A discontinuous chain of mountains, consisting of discrete angular blocks with apparently random orientations and sizes up to 40 km across and 5 km high, extends for hundreds of kilometers along the west margin of SP. Those in the south are often separated by embaying materials, whereas those in the north, particularly the northernmost al-Idrisi Montes (AIM, Fig. 2), have minimal separation. At AIM, blocks are closely packed, and many blocks have flat or gently sloping upper surfaces with linear textures similar to those of some of the surrounding highland terrain, suggesting breakup of a preexisting surface.

The northern interblock material has a distinctive reddish color (Fig. 2A), contains many smaller blocks, and is slightly elevated relative to SP; similar terrain surrounds some of the mountains to the south. The AIM region contains two depressions floored largely by this finer, interblock material and small blocks ("c" in Fig. 2), and another occupied by a small plain with similar texture and color to that of SP ("e" in Fig. 2). An inward-facing terrace surrounds this depression ("d" in Fig. 2), suggesting an earlier, higher level of plains material.

It was argued by (*5*) that the steep slopes and high elevations of the mountain blocks require a water-ice–based composition; this has now been confirmed spectroscopically (*8*). Like the angular blocks in europan chaos, Pluto's mountain blocks appear to consist of fragments of preexisting ice crust that have been detached by fracturing, transported, and rotated. The exclusive location of this

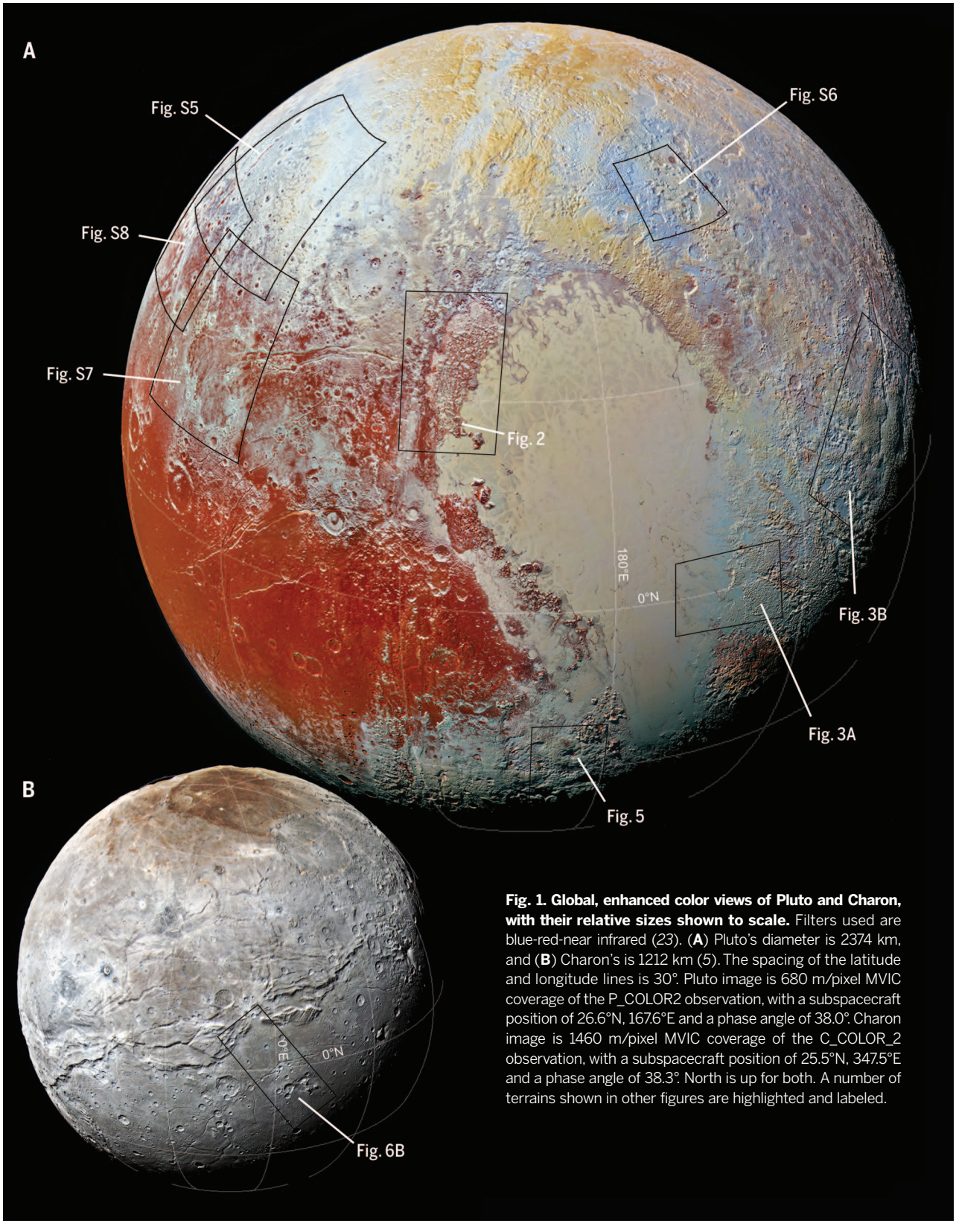

Fig. 1. Global, enhanced color views of Pluto and Charon, with their relative sizes shown to scale. Filters used are blue-red-near infrared (*23*). (**A**) Pluto's diameter is 2374 km, and (**B**) Charon's is 1212 km (*5*). The spacing of the latitude and longitude lines is 30°. Pluto image is 680 m/pixel MVIC coverage of the P_COLOR2 observation, with a subspacecraft position of 26.6°N, 167.6°E and a phase angle of 38.0°. Charon image is 1460 m/pixel MVIC coverage of the C_COLOR_2 observation, with a subspacecraft position of 25.5°N, 347.5°E and a phase angle of 38.3°. North is up for both. A number of terrains shown in other figures are highlighted and labeled.

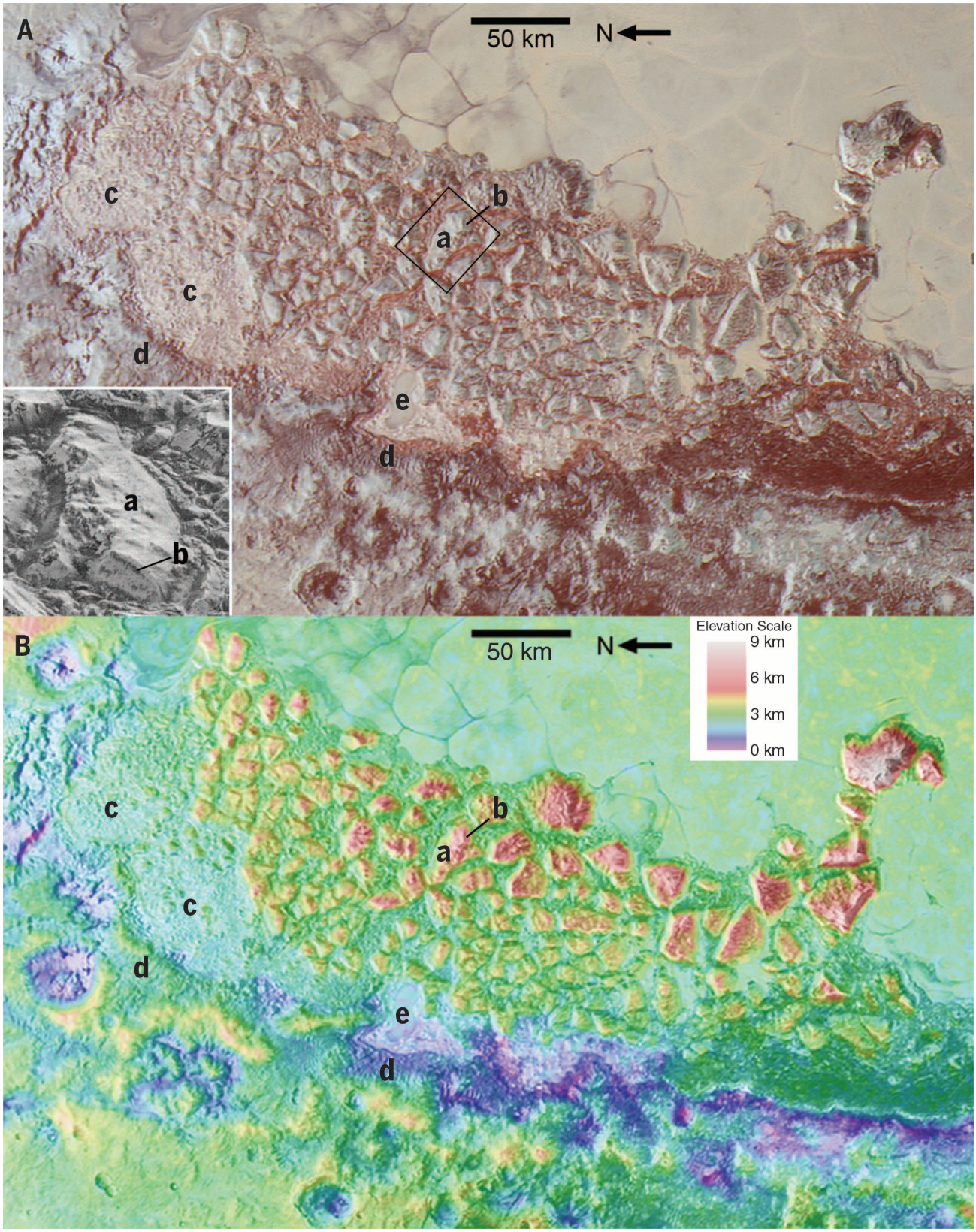

Fig. 2. The chaotic mountains of al-Idrisi Montes on the northwest margin of SP. (**A**) Image is 680 m/pixel, reprojected, MVIC enhanced color coverage of the P_COLOR2 observation, centered at 34.5°N, 155°E. The 30 by 40 km–wide inset shows a detail of one mountain in 79 m/pixel, LORRI coverage of the P_MVIC_LORRI_CA observation. (**B**) Colorized digital elevation model (DEM) overlain on the 680 m/pixel MVIC coverage. (a) Textured surface possibly predating block formation; (b) steep fracture surface with possible exposed layering; (c) chaos composed of small blocks; (d) inward-facing terraces; (e) small exposure of SP-like material.

chaotic, blocky mountainous terrain on the margins of SP (fig. S3), which evidently contains a substantial thickness of low-viscosity ices, makes it plausible that these latter ices play a role in the disruption of Pluto's crust.

H_2O ice is buoyant with respect to N_2 and CO ice, but not CH_4 ice, and blocks of H_2O ice embedded or buried in solid N_2 and/or CO will tend to rise isostatically. Small blocks can be carried along by convective or advective motions, essentially as icebergs, and large blocks may be undermined, shifted, and rotated. If the solid N_2/CO ice is sufficiently deep, then several of the smaller mountains may be floating within the plains, although the reliefs of the largest mountains (2 to 3 km), which skirt the western margin of SP, implies that their keels are likely "grounded" on the basement (supplementary materials). Why mountainous terrains within SP are limited to its western margin is unknown.

Pits, blades, plains, and glaciers east of SP

An intricate, high-albedo, 500-km-wide landscape of pitted uplands and smooth plains, bordered by lower-albedo bladed terrain, forms most of the eastern portion of Tombaugh Regio (TR).

Pitted uplands: The dominant features are pits ("a" in Fig. 3A), most of which are a few kilometers across, but some exceed 25 km, locally intersecting to form long, linear troughs. Based upon preliminary topography, pits average ~1 km deep. The crests of the pits define an undulating upland surface 2 to 4 km above SP. In parts of the uplands, the pitting is organized into distinct northeast-southwest–trending ridge-and-trough terrain with ~5-km crest-to-crest spacing. The sidewalls of the pits typically slope up to 30°, suggesting that rigid material underlies the thin, bright surface layer.

Bladed terrain: The pitted uplands transition northeastward to several broad (~100-km-wide) swells named Tartarus Dorsa (TD), whose flanks and crests are covered with numerous roughly aligned blade-like ridges oriented approximately north-south (Fig. 3B). Individual ridges are typically several hundred meters high and are spaced 5 to 10 km crest to crest, separated by V-shaped valleys with slopes of ~20°. Many ridges merge at acute angles to form Y-shape junctions in plan view. Along the west flank of TD are a number of triangular-to-rectangular facets of the plains that ramp upward toward the east.

Smooth plains: Nearly level expanses of smooth plains up to 50 km across occur at relative low points in the pitted uplands as well as elevated terraces adjacent to SP ("b" in Fig. 3A). They are generally smooth at 300 m/pixel resolution, but locally collections of kilometer-scale hills extend above the plains, probably as protrusions or embedded fragments of the pitted terrain material. The smoothness of the level plains suggests that they are composed of deformable ices, probably similar in composition to SP.

Glaciers: At a few locations along the SP–pitted uplands boundary, smooth materials connect with SP along the floors of troughs 1.5 to 6 km wide ("b" in Fig. 3A). High-phase imaging of the southernmost of these systems reveals conspicuous medial flow lines within the troughs extending onto SP, with the ice in the troughs sloping 2° to 3° over more than 50 km (supplementary materials). This pattern implies glacial-like flow of the plains material into SP, perhaps analogous to ice streams at the margins of terrestrial ice sheets. At present, it is unresolved whether the flowing ice carved the troughs.

Origins of these terrains: Both the pitted uplands and bladed terrain may be remnants of a formerly continuous deposit degraded either by sublimation (forming features analogous to those of degraded terrestrial snow or ice fields —penitentes and sun-cups—but much larger), or through undermining and collapse, possibly through melting at depth. An additional possibility is growth of ridges through preferential deposition of volatiles on ridge crests, analogous to pinnacle formation on Callisto (*3*). The preferential orientation of troughs and ridges in both terrains suggests an origin influenced by solar illumination direction and/or atmospheric circulation. In the case of the bladed terrain, if the material forming it was exposed through upwarping and erosion, it may have been a once-buried layer. The high albedo of the pitted uplands suggests condensation of volatiles sublimated and transported from SP (the pits that are prevalent on south SP may form through sublimation of N_2 ice; see supplementary materials); these volatiles may accumulate to form the smooth plains.

Upland terrains: Washboard and dissected terrains

The uplands north and northwest of SP contain a variety of morphologies, notably including expanses of parallel ridges and troughs that we call washboard terrain, and dissected terrain locally organized into valley networks. Fretted terrain and eroded mantles are discussed in the supplementary materials.

Washboard terrain: Many expanses in this region feature parallel ridges and grooves with a crest-to-crest wavelength of about 1 km (Fig. 4A). The ridges retain a consistent northeast-southwest orientation, even where developed on the interior floors of craters. The albedo of washboard surfaces matches that of nearby ungrooved terrain, and underlying terrain features remain visible where grooved. These observations suggest that washboarding is a superficial modification, either by erosion of the underlying surface or, alternatively, as part of a thin regional deposit. The grooving is superimposed on higher-relief topographic features such as ridges, craters, and dissected terrain. Occasional 1- to 2-km-diameter craters are superposed on the washboarding.

Dissected terrain: Terrains dissected by valleys are common on the EH, including fluted, dendritic, plateau, alpine, and mountainous variants (Fig. 4B). Two of these types occur widely. Fluted terrain containing troughs 15 to 20 km across with up to 2-km relative relief that are eroded into broad hills constitute one of these. The troughs or flutes are regularly spaced at 3 to 4 km and are oriented downhill with slopes up to 20°. The interior walls of some craters are similarly fluted. These troughs terminate abruptly in depressions or crater floors without obvious evidence of deposition. Similarly spaced dendritic valley networks are another type of dissected terrain. The networks generally terminate in broad depressions. Dissected terrain appears to postdate and modify the larger upland craters. The other, less common, styles of dissection are described in the supplementary materials.

Origins of these terrains: The mechanisms regulating the characteristic scale and groove orientation of washboarding remain uncertain. In the dissected terrain, both the fluted terrain and the dendritic valley networks probably result from advective processes, most likely flow of nitrogen-rich ice, possibly accompanied by basal melting (supplementary materials). The spatial variation in morphology of the valley networks is likely to be a response to local topographic setting, substrate properties, latitudinal variations in insolation, and variation in depths and durations of N_2 ice accumulation.

Cthulhu Regio (CR)

CR is a large dark area that covers a swath from ~15°N to ~20°S (fig. S1), bordering TR at 160°E, and stretching westward almost halfway around the planet to 20°E. Eastern CR is not a distinct physiographic province, but instead a region of dark mantling thin enough to preserve underlying topography, superimposed upon various geological terrains, including dendritic valleys, craters, fossae (long, narrow troughs), and retreating scarps. The dark coating is likely the result of atmospheric tholin deposition (*8*). CR contains striking correlations between color/albedo and topography: Bright material is correlated with high elevations in some areas and with north-facing slopes in others. This may result in part from insolation-dependent deposition of the bright material on the dark landscape. Other western low-latitude terrains are discussed in the supplementary materials.

Large mounds with central depressions

Southwest of Norgay Montes (figs. S1C and S3) are two broad quasicircular mounds (Fig. 5). The northernmost (Wright Mons, WM) is 3 to 4 km high and ~150 km across. At its summit is a central depression at least 5 km deep that has a rim showing concentric fabric. The mound surface has a hummocky, blocky surface texture and is very lightly cratered. A similar but even larger feature (Piccard Mons, PM) is seen in twilight stereo imaging 300 km to the south. This reaches ~6 km high and 225 km across. The general shapes of these edifices and associated structures appear to be constructional. Their origin could involve cryovolcanism (*3*), but entailing materials considerably stronger than N_2 ice.

Tectonics

Pluto's EH shows numerous belts of aligned, often arcuate, troughs and scarps that can reach several hundred kilometers in length and several

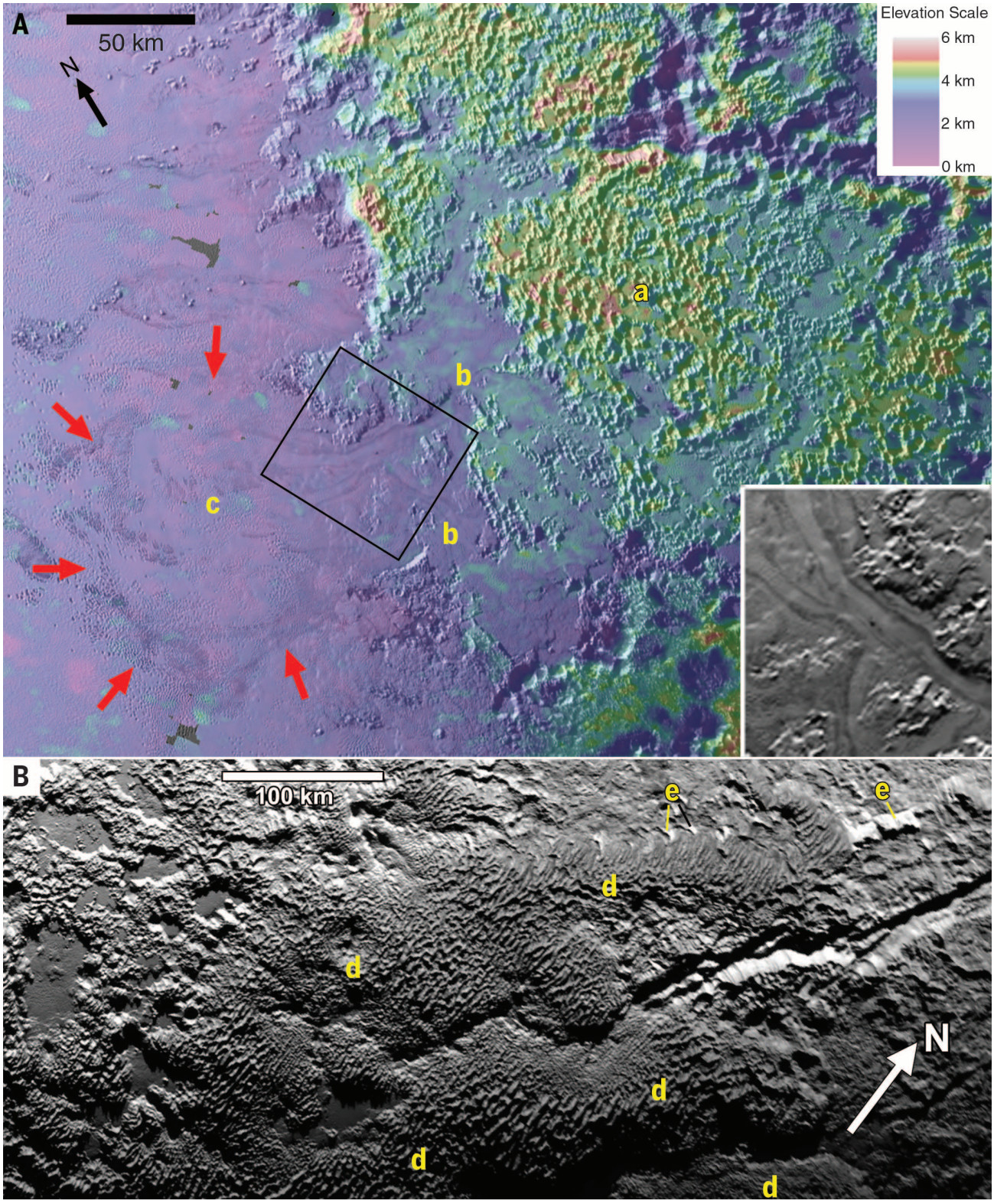

Fig. 3. Pitted uplands, glaciers, and bladed terrain. (**A**) Colorized DEM of pitted uplands and valley glaciers east of SP, overlain on 320 m/pixel, reprojected MVIC coverage of the P_MVIC_LORRI_CA observation, centered at 2°N, 195.5°E. (a) Densely pitted terrain, with smooth material covering the floors of the pits. (b) Smooth plains exhibiting glacial flow through notches in the pitted uplands toward SP. The 60 by 50 km–wide rotated inset enhances the contrast of the original MVIC image to emphasize flow lines. (c) Debouchment of a valley glacier into SP, where it assumes the lobate planform of a piedmont glacier. Possible outer flow edges are indicated by red arrows. (B) Bladed terrain outcropping on top of several broad swells (marked with "d") of Tartarus Dorsa. Image is 680 m/pixel, reprojected MVIC coverage of the P_COLOR2 observation, centered at 17.5°N, 227°E. (e) Triangular and rectangular facets of the plains ramping upwards onto the ridges.

kilometers high, and which are often observed to cut across preexisting landforms as well as branch into one another (fig. S9 and supplementary materials). We interpret these features to be extensional fractures (graben and normal faults) in varying stages of degradation. Notable is the single 3- to 4-km-deep V-shaped trough, Virgil Fossa (VF, fig. S9C), which has unbroken segments of at least 200 km and an asymmetric upward displacement on the south scarp of 1 to 2 km. Toward the trough's eastern end, it cuts through Elliot crater, and to the west links with a network of smaller, subparallel fractures. The high scarp has an anomalously red color and is associated with water ice (*8*). Other extensional fracture systems are shown in fig. S9.

Compressional features, if present, are less obvious. One candidate, TD (figs. S9F and 3B), consists of several elongated swells ~200 km wide, traversed by at least one long, prominent extensional feature (Sleipnir Fossa). TD could be due to compressional folding, but may also be analogous to a salt-cored anticline or arch, in which low-density core material contributes to the arching.

The differing fault trends and states of degradation suggest multiple deformation episodes and prolonged tectonic activity. We do not elaborate on their origin here, but note that equatorial normal faults would not arise from despinning stresses alone (*9*). The great length of individual faults on Pluto, their scarp steepness (>20°, from stereo), spectral evidence (*8*), and the absence of localized flank uplift strongly suggest a thick water-ice lithosphere (as opposed to a thin water-ice lithosphere, or one made of any of Pluto's volatile ices).

Impact craters

Pluto displays a wide variety of crater sizes and morphologies (figs. S11 and S12; supplementary materials). Globally, recognizable crater diameters range from ~0.5 to 250 km, not including any possible ancient basin underlying SP. Crater densities

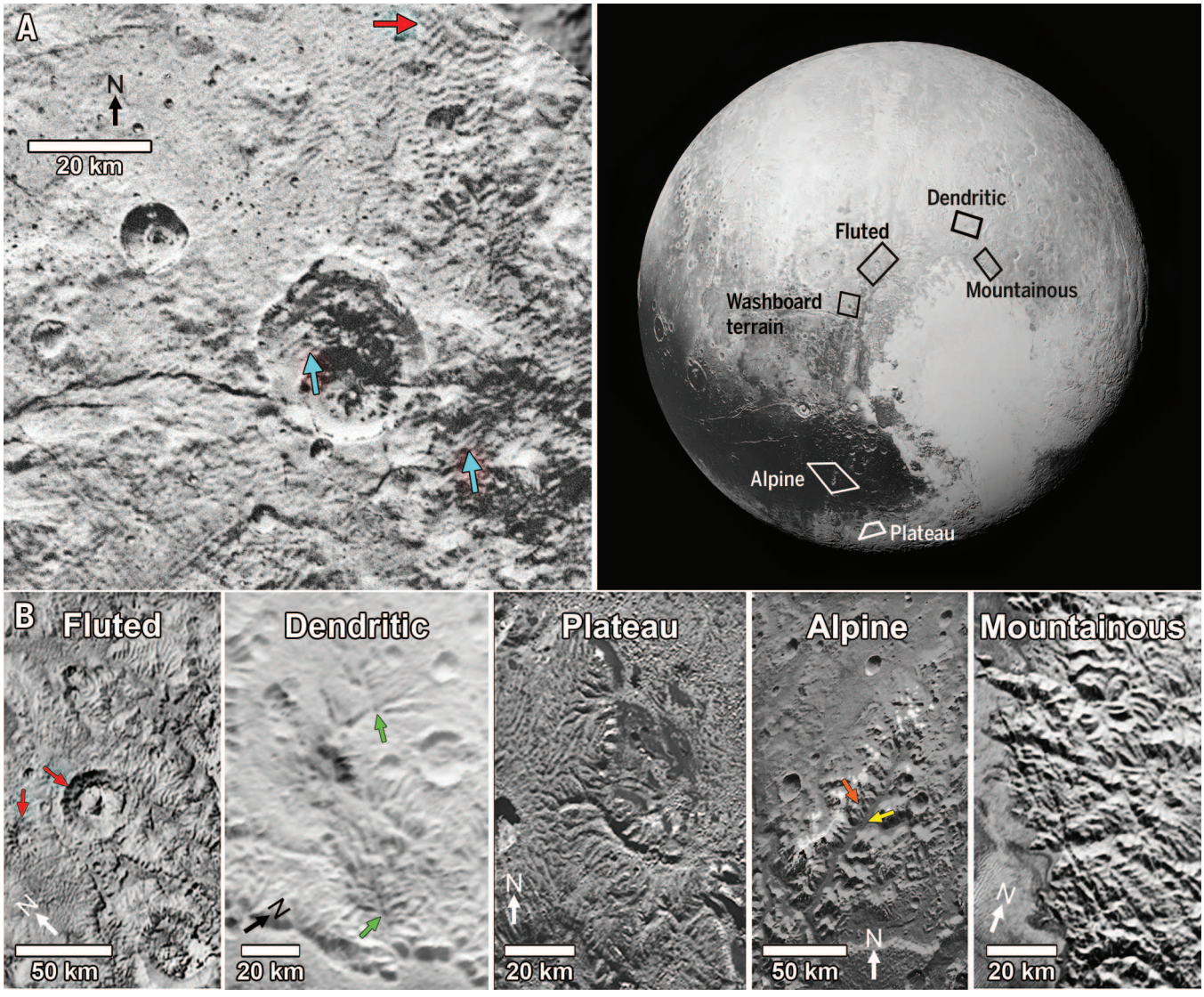

Fig. 4. Washboard and dissected terrains on Pluto. Locations of the terrains are highlighted at upper right. (**A**) Washboard terrain northwest of SP. Image is 125 m/pixel, reprojected, LORRI coverage from the P_MPAN_1 observation, centered at 38°N, 145.5°E. Blue arrows indicate washboard texture within craters, and the red arrow indicates where washboard terrain has modified fluted terrain. (**B**) The five types of dissected terrains with informal typology discussed in the text and supplementary materials. Fluted, dendritic, and mountainous terrain images are taken from 680 m/pixel, reprojected MVIC coverage of the P_COLOR2 observation; plateau and alpine terrain images are taken from 320 m/pixel MVIC coverage of the P_MVIC_LORRI_CA observation. The fluted terrain image is centered at 48.4°N, 153.4°E. Red arrows indicate incision of downslope-oriented grooves. The image of dendritic valley networks (green arrows) is centered at 54.8°N, 186.6°E. The dissected plateaus image is centered at 22.1°S, 155.6°E. Alpine valley systems show wide, dendritic trunk valleys (yellow arrow) that head on dissected mountainous slopes (orange arrow); image is centered at 5.2°S, 146.5°E. The mountainous dissection image is centered at 45.4°N, 188.9°E.

vary widely on Pluto, from the heavily cratered portions of CR, to SP, which has no identifiable impact craters. The total cumulative crater size–frequency distribution (SFD) on the EH is shown in fig. S13A. From this, we conclude that Pluto's surface as a whole dates back nearly to the time of the end of Late Heavy Bombardment (LHB), or in the context of the Kuiper belt, the proposed era of rearrangement of the outer solar system [perhaps 4 billion years ago; e.g., (*10*)]. On the EH, only the eastern portion of CR appears to approach the saturation crater densities (for large craters, compare fig. S13B) that would be expected of a terrain that survived from the LHB itself, when cratering rates were likely much higher than at present. In contrast, TD, eastern TR, the water-ice mountain ranges, the mounds (all very lightly cratered), and especially SP (no identified craters) are all very young (fig. S13C). No craters have been detected in SP down to 2-km diameter, which is a tighter size limit than reported previously (*5*) and implies a model crater retention age of no greater than ~10 million years, and possibly much less (*11*) (supplementary materials).

Geologic evolution

Though complex and largely novel, landforms on Pluto present many clues to their origin and history. The basin in which SP is located is ancient, despite the youthfulness of its interior deposits. Its semicircular rim of elevated mountainous terrains suggests that it probably is a heavily modified impact basin. The larger visible craters in

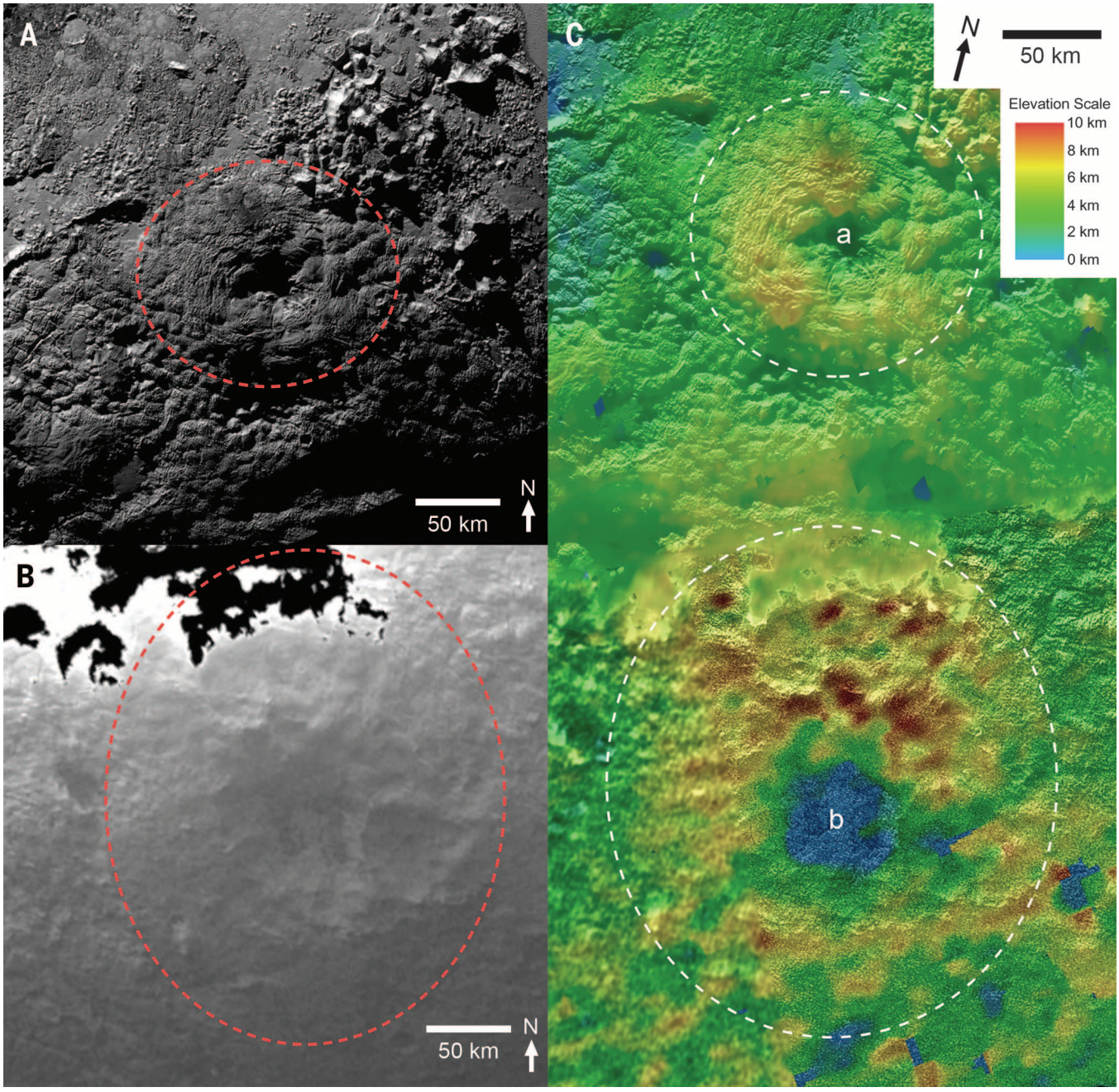

Fig. 5. Quasicircular mounds south of SP, both with depressions at their summits, which may have a cryovolcanic contribution. Dashed lines mark their approximate boundaries. Image is 320 m/pixel, reprojected MVIC coverage of the P_MVIC_LORRI_CA observation. (**A**) Wright Mons at 22°S, 173°E. (**B**) Piccard Mons at 35°S, 176°E, seen in twilight. (**C**) Colorized DEM overlain on the MVIC coverage of the mounds. "a" marks Wright Mons, "b" marks Piccard Mons.

these mountainous terrains probably postdate this SP basin.

Except in the west, the uplands surrounding SP have been blanketed with mantles of substantial thickness and various surface compositions (*8*), which have been partially stripped. The primary agents of upland modification probably include sublimation, frost deposition, and glacial erosion. We envision two end-member scenarios: In one, a formerly deep ice mantle (largely N_2) covered the uplands surrounding SP but was gradually lost to space. As ice levels dropped, glacial ice eroded the dissected terrains and, to the east of SP, flowed back into SP, leaving remnants in smooth-floored depressions. Alternatively, ices may have been cycled between SP and its surroundings, perhaps episodically, to form the glaciers and dissected terrains. In this case, loss to space of volatile ices need not have occurred (*12*). Nitrogen and other volatiles available to the surface environment may also be replenished episodically by sources within Pluto's interior (*13*).

The dark mantles of CR and other local regions conform to present topography, suggesting that they postdate the erosional sculpting of the landscape or are actively recycled. The cellular pattern imposed on SP ices is a relatively young feature, given the absence of craters, and the hectometer-scale pits and ridges on SP constitute the youngest widespread landforms on Pluto.

The relative youth of some extensional features is consistent with predicted recent extensional stresses associated with a late, possibly partial freezing of a subsurface ocean (*14*), though other explanations are also possible. Various lines of evidence, including the spectroscopic identification of water ice along the exposed walls of VF, as well as the steep, chaotic mountains bordering SP, suggest a cold, strong, water ice–based crust.

Charon

Charon's EH (Fig. 1B) can be divided into two broad provinces separated by an assemblage of ridges and canyons, which span the EH from east to west. North of this tectonic belt is rugged, cratered terrain; south of it are smoother but geologically complex plains. The northern hemisphere is capped by the dark, reddish Mordor Macula (MM). Relief exceeding 20 km is seen in limb profiles and stereo topography (fig. S16), and is a testament to the bearing strength of cold water ice and Charon's modest surface gravity [0.29 m s^{-2} (*15*)].

Cratered northern terrain

Charon's northern terrain is exceptionally rugged, and contains both a network of polygonal troughs 3 to 6 km deep, and a possibly related irregular depression almost 10 km deep immediately south of the edge of MM near 270°E (fig. S14). A prominent, ~230-km-diameter, 6-km-deep crater (Dorothy Gale) at 58°N, 38°E (fig. S2) straddles the discrete edge of MM (*5*). The cumulative crater distribution for Charon's northern terrain is shown in fig. S14A. The crater density at large sizes, for which counts are reliable, implies a surface age older than ~4 billion years (Gy) (supplementary materials).

The overall dark deposit of MM does not correlate with any specific terrain boundary or geologic unit. A prominent, arcuate ridge ~5 km high ("a" in fig. S14) coincides with a prominent albedo and color boundary (compare fig. S14 with Fig. 1B) and may be an impact basin rim or an extension of the tectonic deformation seen more clearly to the south. Other morphological indicators of an impact origin, such as a well-defined ejecta blanket or secondary craters, have not been discerned.

Ridges, troughs, and canyons

The structural belt that bisects Charon's EH consists of subparallel scarps, ridges, and troughs of variable extent, but over 200 km wide in places (Fig. 1B). Notable are two chasmata: (i) Serenity Chasma, which is >50 km wide and ~5 km deep, and exhibits a pronounced rift-flank uplift; and (ii) Mandjet Chasma, which appears to be fault bounded and reaches ~7-km depth (fig. S2). These chasmata resemble extensional rifts on several mid-sized icy satellites (*9*).

We interpret this assemblage as the structural expression of normal faults and graben that represent substantial, aligned, tectonic extension of Charon's icy crust. Several large craters superposed on the chasmata indicate that this extension is geologically old (see below and fig. S15). Given the horizontal and vertical scale of these structures, steeply dipping normal faults likely extend to depths of tens of kilometers. They represent global areal extension on the order of ~1%.

Southern plains

The smoother southern half of Charon's EH forms an apparently continuous surface with low relief named Vulcan Planum (VP). Near the bounding scarps to the north, the planum slopes gently downward by ~1 km toward the scarps. Portions of the plains observed at higher resolution exhibit a distinctive, lineated texture of closely spaced grooves or furrows (fig. 6B). One possible origin for the southern plains is tectonic resurfacing like that seen on the icy satellites Ganymede and Enceladus (*3*). Morphologically distinct groups of deeper, rille-like narrow troughs and furrows that postdate the plains also occur. Although deep, these troughs are nonetheless superimposed by a number of impact craters, and thus are themselves relatively old. The en echelon nature of these troughs, and rough parallelism with the chasmata to the north, suggests a tectonic origin or structural control.

Fields of small hills (2 to 3 km across), areas of relatively low crater density, and at least one pancake-shaped unit are consistent with cryovolcanic resurfacing (fig. 6B) (*16*). Peaks surrounded by "moats" (Kubrick and Clarke Montes, KM and CM; see fig. S2 and "b" labels in Fig. 6A) were noted by (*5*). The peaks are up to 3 to 4 km high above the floors of the moats, and the moats 1 to 2 km deep below the surrounding plains. The moat at CM appears to expose a more rugged terrain ("j" label in Fig. 6B), with smooth plains embaying the margins, two of which are lobate. The moats are perhaps due to mountain loading and flexure of Charon's lithosphere. There are two additional depressions surrounded by rounded or lobate margins ("a" labels in Fig. 6A); thus alternatively, both the moats and depressions may be the expressions of the flow of, and incomplete enclosure by, viscous, cryovolcanic materials, such as proposed for the uranian moons Ariel and Miranda (*3*, *17*).

The SFD of impact craters on the southern plains lies below that for the north at large diameters (≥50 km, fig. S15A), yet model ages for the plains point to an age of ~4 Gy (supplementary materials), thus implying an older age for the northern terrain, and a similar or older age for those chasmata that predate (were resurfaced by) VP. In limited regions on VP, however, craters are sparse (Fig. 6B), implying that the resurfacing of VP may have acted over an extended time. The crater SFD of VP is also likely the truest expression of the Kuiper belt impact crater production function for the Pluto system (*5*), and one that appears to rule out certain classes of Kuiper belt object population size distributions (supplementary materials).

Geological evolution

Charon's surface is dominated by impacts, tectonic deformation, and resurfacing, and as such fits broadly into the accepted picture of geologic evolution on icy satellites (*18*, *19*). That Charon is so geologically complex, however, would seem to require a heat source for reshaping what would have otherwise been a heavily cratered surface. If the ~4-Gy age of even the youngest of Charon's surfaces is correct, then this activity dates back to an early warmer epoch. The tectonic record is consistent with global expansion, and the smooth plains consistent with the mobilization of volatile ices from the interior. The spatial distribution of tectonic features is not readily reconciled with the kinds of patterns expected (indeed, predicted) from tidal or despinning stresses (*3*). Charon may have had an ancient subsurface ocean that subsequently froze, which would generate the global set of extensional features, and might permit eruption of cryovolcanic magmas (*20*).

A divergent binary

Pluto and Charon are strikingly different in surface appearance, despite their similar densities and presumed bulk compositions (*5*). With the possible exception of MM, the dynamic remolding of landscapes by volatile transport seen on Pluto is not evident on Charon, whose surface is instead dominated spectrally by the signature of water ice (*8*). Whether this is because Charon's near-surface volatile ices have sublimated and have been totally lost to space owing to that body's lower gravity (*21*), or whether something more fundamental related to the origin of the binary and subsequent internal evolution (*22*) is responsible, remains to be determined.

Much of what we see on Pluto can be attributed to surface-atmosphere interactions and the mobilization of volatile ices by insolation. Other geological activity requires or required internal heating. The convection and advection of volatile ices in SP can be powered by present-day radiogenic heat

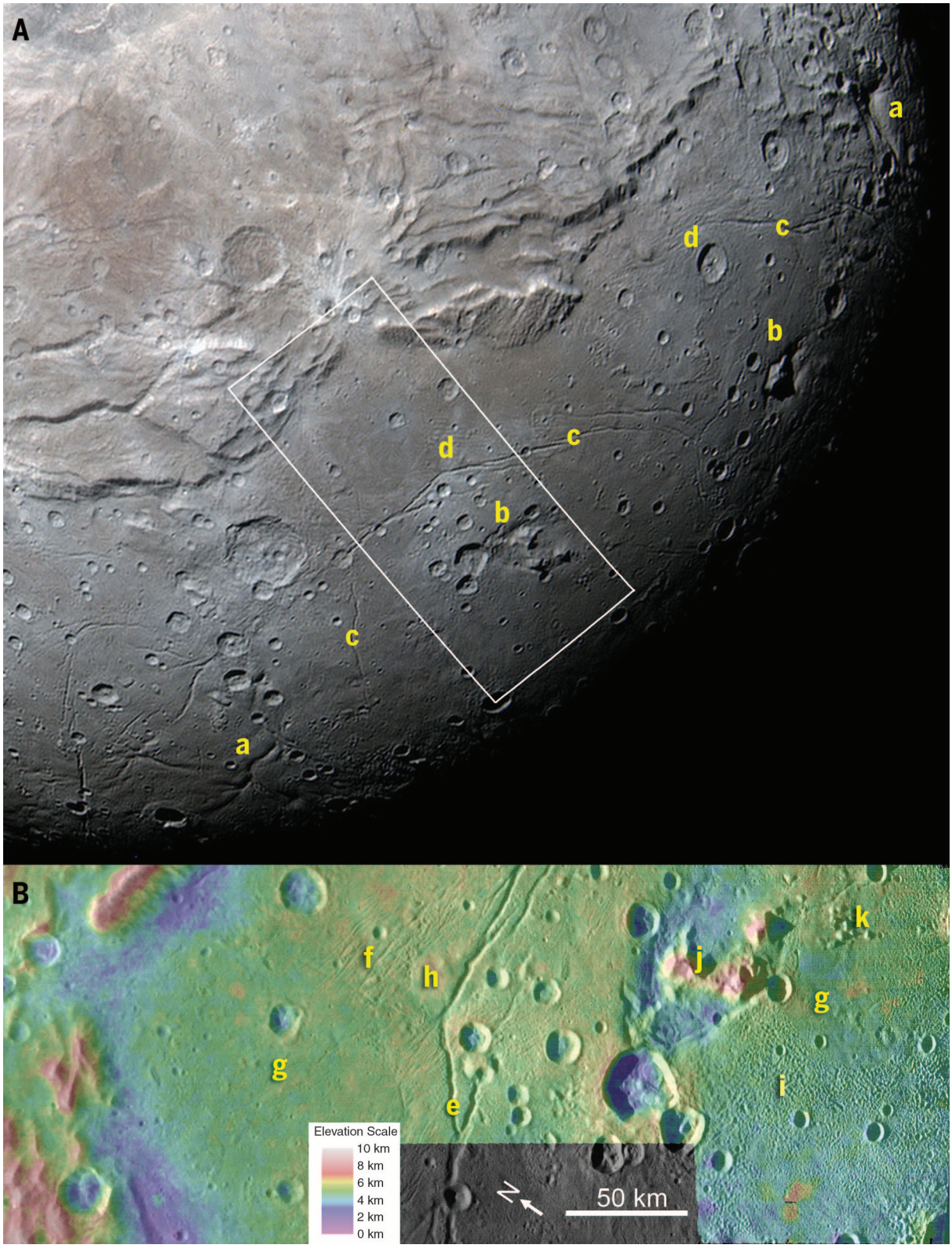

Fig. 6. Enlargement of a portion of Fig. 1B showing details of Vulcan Planum on Charon. (**A**) Image is 1460 m/pixel MVIC coverage from the C_COLOR_2 observation, centered at 5.5°N, 3°E, with north up. (a) Depressions with lobate margins; (b) mountains surrounded by moat-like depressions; (c) deep, rille-like troughs; and (d) shallow, finely spaced furrows. White outline indicates high-resolution image in (B). (**B**) High-resolution view of resurfacing on Vulcan Planum. Image is 160 m/pixel, reprojected LORRI coverage from the C_MVIC_LORRI_CA observation centered at 0°N, 0.5°E, with DEM color overlain. Seen in this LORRI view are rille-like troughs (e) and more finely spaced, shallow furrows (f), smoother regions of lower crater density (g), a pancake-shaped deposit (h), and unusual textured terrain (i). Clarke Mons (j) lies in a depression, which is itself bordered on two sides by distinctive lobate scarps. (k) A field of small hills.

loss (supplementary materials). However, the prominent mountains at the western margin of SP, and the strange, multikilometer-high mound features to the south are both young geologically and presumably composed of relatively strong, water-ice–based geological materials. Their origin, and what drove their formation so late in solar system history, remain uncertain. What is more certain is that all three major Kuiper belt bodies (past or present) visited by spacecraft so far—Pluto, Charon, and Triton—are more different than similar and bear witness to the potential diversity awaiting the future exploration of their realm.

REFERENCES AND NOTES

1. H. A. Weaver, W. C. Gibson, M. B. Tapley, L. A. Young, S. A. Stern, *Space Sci. Rev.* **140**, 75–91 (2008).
2. L. A. Young *et al.*, *Space Sci. Rev.* **140**, 93–127 (2008).
3. J. M. Moore *et al.*, *Icarus* **246**, 65–81 (2015).
4. Materials and methods are available as supplementary materials on *Science* Online.
5. S. A. Stern *et al.*, *Science* **350**, aad1815 (2015).
6. J. Eluszkiewicz, D. J. Stevenson, *Geophys. Res. Lett.* **17**, 1753–1756 (1990).
7. Y. Yamashita, M. Kato, M. Arakawa, *Icarus* **207**, 972–977 (2010).
8. W. M. Grundy *et al.*, *Science* **351**, aad9189 (2016).
9. G. C. Collins *et al.*, in *Planetary Tectonics*, R. A. Schultz, T. R. Watters, Eds. (Cambridge Univ. Press, New York, 2010), pp. 264–350.
10. R. Gomes, H. F. Levison, K. Tsiganis, A. Morbidelli, *Nature* **435**, 466–469 (2005).
11. S. Greenstreet, B. Gladman, W. B. McKinnon, *Icarus* **258**, 267–288 (2015).
12. G. R. Gladstone *et al.*, *Science* **351**, aad8866 (2016).
13. K. N. Singer, S. A. Stern, *Astrophys. J.* **808**, L50 (2015).
14. G. Robuchon, F. Nimmo, *Icarus* **216**, 426–439 (2011).
15. M. Brozović, M. R. Showalter, R. A. Jacobson, M. W. Buie, *Icarus* **246**, 317–329 (2015).
16. P. M. Schenk, J. M. Moore, in *Solar System Ices*, B. Schmitt, C. de Bergh, M. Festou, Eds. (Kluwer Academic, Dordrecht, Netherlands, 1998), pp. 551–578.
17. D. G. Jankowski, S. W. Squyres, *Science* **241**, 1322–1325 (1988).
18. L. M. Prockter *et al.*, *Space Sci. Rev.* **153**, 63–111 (2010).
19. G. Schubert *et al.*, *Space Sci. Rev.* **153**, 447–484 (2010).
20. M. Manga, C.-Y. Wang, *Geophys. Res. Lett.* **34**, L07202 (2007).
21. E. L. Schaller, M. E. Brown, *Astrophys. J.* **659**, L61–L64 (2007).
22. W. B. McKinnon, in *Treatise on Geophysics*, G. Schubert, Ed. (Elsevier, Amsterdam, ed. 2, 2015), vol. 10, pp. 637–651.
23. D. C. Reuter *et al.*, *Space Sci. Rev.* **140**, 129–154 (2008).

ACKNOWLEDGMENTS

We thank the many engineers who have contributed to the success of the New Horizons mission and NASA's Deep Space Network for a decade of excellent support to New Horizons. We thank the reviewers for close and meticulous reading, and P. Engebretson for contribution to figure production. S.A.S. is also affiliated with Florida Space Institute, Uwingu LLC, Golden Spike Co., and World View Enterprises. H.J.R. is also affiliated with B612 Foundation and Cornell Technical Service. Supporting imagery is available in the supplementary materials. As contractually agreed to with NASA, fully calibrated New Horizons Pluto system data will be released via the NASA Planetary Data System at https://pds.nasa.gov/ in a series of stages in 2016 and 2017 as the data set is fully downlinked and calibrated. This work was supported by NASA's New Horizons project.

SUPPLEMENTARY MATERIALS

www.sciencemag.org/content/351/6279/1284/suppl/DC1
Materials and Methods
Supplementary Text
Figs. S1 to S15
Table S1
References (*24*–*83*)

16 November 2015; accepted 11 February 2016
10.1126/science.aad7055

FEEDING BEHAVIOR

The nutrient sensor OGT in PVN neurons regulates feeding

Olof Lagerlöf,[1,2] Julia E. Slocomb,[3] Ingie Hong,[1] Yeka Aponte,[1,4] Seth Blackshaw,[1] Gerald W. Hart,[2] Richard L. Huganir[1]*

Maintaining energy homeostasis is crucial for the survival and health of organisms. The brain regulates feeding by responding to dietary factors and metabolic signals from peripheral organs. It is unclear how the brain interprets these signals. O-GlcNAc transferase (OGT) catalyzes the posttranslational modification of proteins by O-GlcNAc and is regulated by nutrient access. Here, we show that acute deletion of OGT from αCaMKII-positive neurons in adult mice caused obesity from overeating. The hyperphagia derived from the paraventricular nucleus (PVN) of the hypothalamus, where loss of OGT was associated with impaired satiety. These results identify O-GlcNAcylation in αCaMKII neurons of the PVN as an important molecular mechanism that regulates feeding behavior.

Obesity is a major contributor to disease throughout the world (*1*). Currently, there is no successful and available treatment for the majority of obese patients. One of the genes most commonly linked to human obesity, *Gnpda2*, affects flux through the hexosamine biosynthesis pathway (HBP) (*2*–*4*). The HBP produces uridine-diphosphate: N-acetylglucosamine (UDP-GlcNAc), which is the donor substrate for the enzyme O-GlcNAc transferase (OGT). OGT cleaves UDP-GlcNAc and covalently attaches GlcNAc to the hydroxyl group of serine or threonine in nuclear and cytoplasmic proteins in β-linkage (O-GlcNAc). Nutrient access directly via the HBP, and metabolic hormones such as insulin regulate the activity of OGT (*5*, *6*). Although OGT has been shown to be important for neuronal development, the role of OGT for mature brain function is almost completely unknown (*7*–*9*). To study the function of OGT in normal behavior, we created conditional OGT knockout mice by crossing floxed OGT mice (OGT^{Fl}) with mice expressing a tamoxifen-inducible version of Cre recombinase under the αCaMKII promoter (αCaMKII-$CreER^{T2}$). This enables acute brain-specific deletion of OGT in αCaMKII-expressing neurons in adult mice, which we confirmed by means of immunohistochemistry, Western blotting, and polymerase chain reaction (fig. S1). Knockout of OGT in other tissues and cells has been shown to lead to decreases in cell number, probably because of impaired mitosis, and in fact, constitutive knockout of OGT leads to early embryonic lethality (*8*, *10*, *11*). In contrast, in post-mitotic neurons deletion of OGT did not affect cell number in vitro or in vivo (fig. S2, A and B).

Acute and brain-specific loss of OGT in adult mice caused rapid weight gain (Fig. 1, A and B, and fig. S3, A and B). Within 3 weeks, the amount of adipose tissue tripled, whereas the lean weight had not changed, as quantified with whole-body nuclear magnetic resonance (NMR) [fat mass, n = 7 wild-type (WT) mice, 2.5 ± 0.21 g; n = 6 OGT knockout mice, 8.3 ± 0.86 g] (fig. S3, C and D). The incorporation of fat was general and not particular to any specific body region (fig. S3, E to G). Obesity can result from either excessive caloric intake or insufficient energy expenditure. Daily food intake rapidly increased upon knockout of OGT and plateaued at a level more than twice as high (Fig. 1C). If access to food was restricted to the same amount consumed by WT mice, the OGT knockout mice retained normal body weight. When free access to food was reintroduced, the OGT knockout mice quickly approached the weight of OGT knockout littermates who had been fed ad libitum throughout the experiment (Fig. 1D). To quantify food intake and energy expenditure simultaneously in real time, we used comprehensive laboratory animal monitoring system (CLAMS). CLAMS confirmed that loss of OGT leads to hyperphagia (fig. S3H). Energy expenditure was actually increased (fig. S3I). The accelerated energy expenditure resulted from, at least in part, hyperactivity (fig. S3J). As expected from a combination of hyperphagia and hyperactivity, knocking out OGT caused higher vO_2 and vCO_2, leading to a respiratory exchange ratio (RER) above 1 (n = 17 WT mouse days (6 mice), 0.94 ± 0.004; n = 20 OGT knockout mouse days (6 mice), 1.04 ± 0.007) (fig. S3, K to M).

Daily food intake is a factor of both the size of each meal and meal frequency. A normal diurnal rhythm was preserved in OGT knockout mice (Fig. 1E and fig. S4, A and B). Although there was no difference in meal frequency, loss of OGT increased meal size as well as meal duration (meal size, n = 268 WT mouse meals (6 mice),

[1]Solomon H. Snyder Department of Neuroscience, Kavli Neuroscience Discovery Institute, Johns Hopkins University School of Medicine, Baltimore, MD 21205, USA. [2]Department of Biological Chemistry, Johns Hopkins University School of Medicine, Baltimore, MD 21205, USA. [3]National Institute on Drug Abuse + National Institutes of Health/Johns Hopkins University Graduate Partnership Program, Baltimore, MD 21224, USA. [4]Intramural Research Program, Neuronal Circuits and Behavior Unit, National Institute on Drug Abuse, Baltimore, MD 21224, USA.
***Corresponding author. E-mail: rhuganir@jhmi.edu**